The Boundary Layer Characteristics of Coastal Urban Environments

Kalimur Rahman[1], Gabriel Rios[2], Harold Gamarro[3], Omar Addasi[1], Jean Carlos Peña[3], Jorge Gonzalez-Cruz[3], Bob Bornstein[4], Prathap Ramamurthy[1]

[1]Department of Mechanical Engineering, Grove School of Engineering, The City College of New York, NY 10031

[2]Program in Atmospheric & Oceanic Sciences, Princeton University, Princeton, NJ 08540-6654

[3]Atmospheric Sciences Research Center, University at Albany-State University of New York, Albany, NY 12226

[4]Department of Meteorology, San Jose State University, San Jose, CA 95192

Corresponding Author: Prathap Ramamurthy
Associate Professor
Department of Mechanical Engineering, The City College of New York, USA
Email: pramamurthy@ccny.cuny.edu
Phone: (212) 650-6326

Abstract:

The atmospheric boundary layer along the coastal-urban transect differs from that of urban or rural regions due to the distinctive interaction between the sea breeze and the urban heat island effect. In this manuscript, we present the observations of the atmospheric boundary layer in the Houston, Texas, area during the Coastal Urban Boundary Layer Experiment (CUBE) from June through September 2022. In order to understand the unique characteristics of the coastal urban boundary layer, we collected mean and turbulence data from micrometeorological towers and ground-based remote sensing instruments installed in the urban, coastal, bay, and rural sections within the greater Houston region. Furthermore, an urbanized weather research and forecast (WRF) model incorporating the Building Effect Parameterization and Building Energy Model (BEP-BEM) scheme is used to recognize the spatial variability of the meteorological conditions in the Houston Metro area. Compared to non-urban sites, the urban site exhibits a higher near-surface temperature throughout the day, with the highest temperature difference occurring at night due to the redistribution of the stored heat as sensible heat. During the dry period in June, we observed comparatively higher sensible heat flux in the urban site, demonstrating the heat island effect and lower latent heat flux due to lack of vegetation. The urban site had higher TKE values throughout the day than other sites because of the uneven roughness of the landscape. One of the unique findings of this study is the shift in spectral characteristics along the coastal-rural-urban transect. The power and co-spectra of zonal and vertical velocities and the vertical heat flux during the convective periods varied significantly across all the sites. The coastal site was influenced mainly by the local bay breeze shifting the peak to higher frequencies. The boundary layer height in the urban site was generally greater than in bay and rural sites due to increased convection in urban areas resulting from anthropogenic modification of land cover and waste heat from air conditioning use. The balance between the urban thermal and mechanical roughness effects was seen during the sea breeze front (SBF) event on the highest heat index day as SBF was triggered and accelerated by UHI.

Keywords: atmospheric boundary layer, Houston, turbulence, urban heat island, sea breeze

1.0 Introduction

The frequency and extent of extreme natural events due to rapid urbanization are significantly influencing various natural and human systems throughout the world (Liu et al. 2022). The Paris Agreement was signed in 2016, with the expressed goal of limiting the long-term rise in global average temperature to 2°C by the year 2100. However, even if the goal of a 1.5°C reduction is met, one-third of the global population is expected to be exposed to extreme weather events, including heatwaves, thunderstorms and hurricanes, frequently (IPCC 2014, Feng et al. 2022). Consequently, residents in coastal urban communities are projected to be disproportionately impacted (Smart et al. 2021). The coastal urban climate is unique due to the interaction between the urban heat island effect and the sea breeze circulation (Childs and Raman 2005, Bauer 2020). The distinct interaction influences both heat and hydrometeorological events. Coastal cities are more prone to heat waves and flooding (Shao et al. 2021, Goyal et al. 2023). In the United States, nearly 75% of the population lives in coastal counties, and globally close to a billion people will

live in coastal urban areas by mid-century (Rosa et al. 2023, Tagtachian and Balk, 2023). Hence, it is extremely vital to understand coastal-urban climatology.

Urban areas contain predominantly impervious surfaces that have higher capacity to absorb heat from the incoming solar radiation. This leads to elevated near-surface air temperature compared to surrounding rural areas throughout the day (Barlow 2014, Meng et al. 2022). This phenomenon is commonly known as the urban heat island effect. Globally, the spatial scale of UHI is on the rise due to the progressive increase of people moving closer to cities to ensure 'privileged' social and economic benefits. Heat islands are known to amplify the impact of heatwaves, worsen air quality, and influence thunderstorms. Understanding the underlying dynamics governing UHI phenomenon is crucial to study how they interact with other local and synoptic scale disturbances (Grotjahn et al. 2016, Gonzalez-Trevizo et al. 2021). Due to the varied land surface geometry and roughness heights, UHI convergence zone is linked to high temperature and significant shear turbulence (Fan et al. 2020). Additionally, coastal urban environments are highly influenced by the sea breeze effect. Previous studies have shown that sea breeze helps moderate the UHI effect and in New York City, Ramamurthy et al. (2017) found that the loss of sea breeze during heatwave episodes was primarily responsible for higher UHI. The interaction between the sea breeze and UHI could potentially impact convection, surface energy balance, cloud formation, thunderstorm initiation, and air quality (Wang et al. 2012, Fan et al. 2018).

As far back as 1989, Yoshikado and Kondo (1989) studied the evolution of the boundary layer under the impact of sea breeze circulation over the urban and suburban areas in Tokyo, Japan. The daytime boundary layer height at the urban site reached 1700 m due to the interaction of sea breeze, wind speed and direction while height at suburban site remained at 600 m. In contrast, Mestayer et al. (2005) investigated the variation in boundary-layer height during sea-breeze episodes in Marseille and noted weakening of the boundary-layer due to sea breeze propagation. Melas et al. (1995) modeled the boundary layer dynamics in Athens where sea breeze coming from Attica peninsula plays a major role in the formation of internal boundary layer within Athens area. Using Doppler sodar and Raman lidar, Casadio et al. (1996) recorded two successive midnight convective occurrences in Rome, Italy, where sea breeze and urban heat island were key contributors to the development of nocturnal convection. During the ESCOMPTE project, Lemonsu et al. (2006) performed a 3-dimensional numerical simulation using the Méso-NH atmospheric model to examine the structure of the boundary layer over Marseille, France, where the boundary layer is influenced by a shallow sea breeze layer overlaid on top of a deep-sea breeze layer. A similar behavior was also discovered by De Tomasi et al. (2011) in Lecce, Italy. Lo et al. (2007) in a model sensitivity study using fifth-generation Mesoscale Model (MM5) investigated the interactions of urban heat island, sea breeze circulation, heat fluxes and air pollution in the Pearl River Delta, China where an enhanced air pollution was associated with sea breeze convergence zone and urban heat island effect. In the SAPUSS project, Pandolfi et al. (2013) looked at the impact of coastal-urban environment on the development of the boundary layer in Barcelona. The development and growth of boundary layer height in Barcelona was significantly influenced by the type of air mass, specifically the cold Atlantic, stagnant regional, and North African advected air masses, and African dust episodes. Melecio-Vázquez et al. (2018) observed the interaction between the maritime boundary layer and the highly convective urban surface layer, which resulted

in the formation of an internal boundary layer in New York city. The boundary layer at the coastal location was changing from a stable to a convective state, whereas the super adiabatic layer was maintained all day at the urban location. Due to local driving mechanisms, Melecio-Vázquez et al. (2018) reported a stable boundary layer at 150 m-200 m level in the coastal-urban environment during clear daytime conditions as opposed to a well-mixed boundary layer seen in rural or non-urban-noncoastal areas.

In Houston, Texas, Haman et al. (2012) used Ceilometer and radiosonde observations to estimate boundary layer height in the Houston area, finding that the height of the daytime boundary layer varied seasonally and ranged from 1100 m to 2000 m while the height of the nocturnal boundary layer remained constant throughout the year between 100 m and 300 m. A mean inversion base height of around 200 m has been recorded in Houston, Texas (Day et al. 2010). Banta et al. (2005), during Texas AQS2000, found a convergence zone close to the urban core due to the interaction between onshore and Seabreeze during the late afternoon hours. The timing and the location of the convergence zone were critical to convection and air quality. Rappenglück et al. (2008) also found the convergence of sea breeze and northerly breeze worsened air quality. Chen et al. (2011) also refer to the key role played by sea breeze and its reversal in Houston. Fan et al. (2020) investigated the interaction of sea breeze and convection from land use change in Houston, Texas utilizing Weather Research and Forecasting model (WRF-Chem) simulations. It was found that land use change and anthropogenic aerosol production due to urban heating from stronger sea breeze circulation causes the rainfall intensity to increase by up to 45% and vertical velocity to increase by up to 75%. Chen et al. (2011) investigated the evolution of sea breeze circulations and the development of stagnant afternoon wind over the Houston area as a result of surface forcings that led to elevated ozone concentrations. The diurnal variability of surface temperature near Houston's urban core was accurately reflected by the model simulations using WRF-UCM, however the diurnal temperature variability in the rural area was underestimated. The study also found that Houston urban core is responsible for the weakening of wind speed and stagnant afternoon wind due to the prevalence of roughness factors in metropolitan area, and that severely dry soil in summer can raise the air temperatures by up to 2°C and change heat flux by up to 50-200 W/m^2. Caicedo et al. (2019) investigated the impact of sea and bay breeze on the evolution of boundary layer and air quality on a high-ozone event during DISCOVER-AQ field campaign using multiple instruments and WRF-Chem simulations. The investigation revealed the impact of sea breeze timing and strength on the localized high ozone pollution at the Galveston Bay. Additionally, two vertical mixing mechanisms are suggested, one from the daytime boundary layer with the nighttime residual layer and the other from the offshore flow to the bay breeze during the ozone episode.

Overall, these studies have highlighted the impact of sea breeze on UHI effects and the general boundary layer dynamics. They have also shown us how the unique characteristics influence air quality. However, the majority of these studies were conducted for a short period and the contrasting dynamics along the coastal-urban-rural transect have not been adequately investigated.

Herein, our primary goal is to investigate how the mean and turbulence characteristics vary along the coastal-urban-rural transect. The results shown here are part of the Coastal Urban Boundary-

layer Experiment (CUBE), which is paired with the Department of Energy's (DOE) Tracking Aerosol Convection Interaction Experiment (TRACER). The primary goal of this article is to understand the difference in mean and turbulent characteristics along the coastal-urban-rural transect.

Data from multiple flux towers and ground-based remote sensing instruments covering the coastal, rural and urban areas are used here. Additionally, the urbanized weather research and forecast model is used to better characterize the spatial variability in key meteorological variables.

2.0 Methods:

2.1 Sites & Instrumentation: The study investigated the variability in surface energy fluxes and boundary layer dynamics at different sites in Houston during the months of June through September 2022. The field sites were located in coastal, urban, and rural settings (Figure 1 shows the location). The University of Houston (UH) North Moody Tower at main campus served as the urban site for flux measurements, UH Coastal Research Center at La Marque in Galveston County served as the coastal site, and UH Sam Houston facilities acted as the rural site, located in Liberty County. Downtown Houston is located around 4 km to the northwest of the North Moody Tower. The UH Coastal Research Center is located around 45 km southeast of the UH North Moody tower. The rural flux station is situated 70 km north-east of the UH North Moody urban flux site. The rural flux tower does not have any exposure to industrial pollution, with at least 41% of the landcover surrounding the site is prime agricultural land [TSHA]. The site also hosts NASA Goddard Space Flight Center Aerosol Robotic Network for aerosol optical depth and boundary layer height estimation. In addition to the three sites, we use data from the primary ARM site situated in La Porte, located by Trinity and Galveston Bay and referred to as Bay in Figure 1. Bay served as the center for the Department of Energy's (DOE) Atmospheric Radiation Measurement (ARM) research project known as the Tracking Aerosol Convection Interaction Experiment (TRACER) which focused on the aerosol-cloud-convection phenomenon within the region. Bay site is around 28 km from the UH North Moody flux tower. Due to its geographic location, it is more vulnerable to industrial pollution. Due to its proximity to the bay, it experiences conditions similar to the coastal site. The site itself is located over a grass field with residential housing nearby. The instrumentation used in these sites is described below.

The Urban site was equipped with a 3-D sonic anemometer and integrated H_2O and CO_2 gas analyzer (IRGASON, Campbell Scientific, USA), sampling data at 10Hz. The 20-ft tall flux towers both at the Coastal and Rural sites hosted an ultrasonic anemometer (Model: CSAT3) and LI-COR eddy covariance system (CS7500, Campbell Scientific, USA). The flux tower at the Bay site operated by Department of Energy Atmospheric Radiation Measurement (ARM) mobile facility (AMF) was an Eddy Correlation Flux Measurement System (ECOR) consisting of 3D sonic anemometer (Windmaster) and an open path infrared gas analyzer (LI-COR, CS7500) (please check Cook and Sullivan, 2020 for more details). A ceilometer (VAISALA, Type CLP311, Helsinki, Finland) and Microwave Radiometer (MP-3000A, serial number: 3071A, Radiometrics Corporation, USA) were collocated at the roof of a Camper Trailer at UH Main campus (i.e., Urban site) to measure the boundary layer heights and vertical profiles of temperature, water vapor, and liquid water up to 10 km. The ceilometer sends laser pulses to the atmosphere to measure the cloud

base and mixing layer heights. The backscattered light intensity from a pulsed indium gallium arsenide (InGaAs) diode laser (910 nm) is used to measure the vertical distance by Vaisala ceilometer (Emeis et al. 2009). Level 3 ceilometer data is resampled over a predetermined time interval (i.e., five minutes) in order to normalize the data rather than using instrument-specific scans. To remove outliers from the boundary layer heights, the N-sigma filter is employed. Lastly, the maximum of the 5-min averaged boundary layer heights is used to get the daily maximum boundary layer height. The ceilometer's accuracy in measuring distance against reflector is greater of ±1% or ±5m. It should be noted that the Microwave radiometers have been found to be inaccurate in monitoring the thermal state of the atmosphere, here we are only using it as a reference. The 10 Hz time series data from the flux towers were continuously recorded to data loggers (Campbell Scientific Loggernet CR 3000). The output of the time series data contains wind components (*Ux*, *Uy*, and *Uz*), sonic temperature (*Ts*), CO_2, H_2O, and ambient pressure. Standard data processing techniques were followed to calculate the mean and turbulence variables. Additionally, data cleaning was performed through outlier removal, which was performed per 3-minute sub-interval by ignoring data >3 standard deviations from the sub-interval mean prior to averaging. Data collected during precipitation events and during intervals when instrument errors were reported were also ignored.

Radiosondes were launched from Coastal, Rural, Bay, and Urban sites to understand the boundary layer characteristics during various time-periods. During the field campaign, a total of 34 radiosonde launches were made, including 25 launches from the Urban, 7 launches from the Coastal site, and 2 launches from the Rural location. Radiosondes have a measurement accuracy of 0.3 to 0.7°C and 5% RH, respectively, for temperature and relative humidity profiles. The radiosondes were launched during heat wave episodes, convective and early morning periods, sea breeze and non-sea breeze days, and Saharan dust plume days. At the Bay site, radiosondes were released at 3-hour intervals during the intensive operative periods (IOPs); for more information refer to the ARM data server (https://adc.arm.gov/).

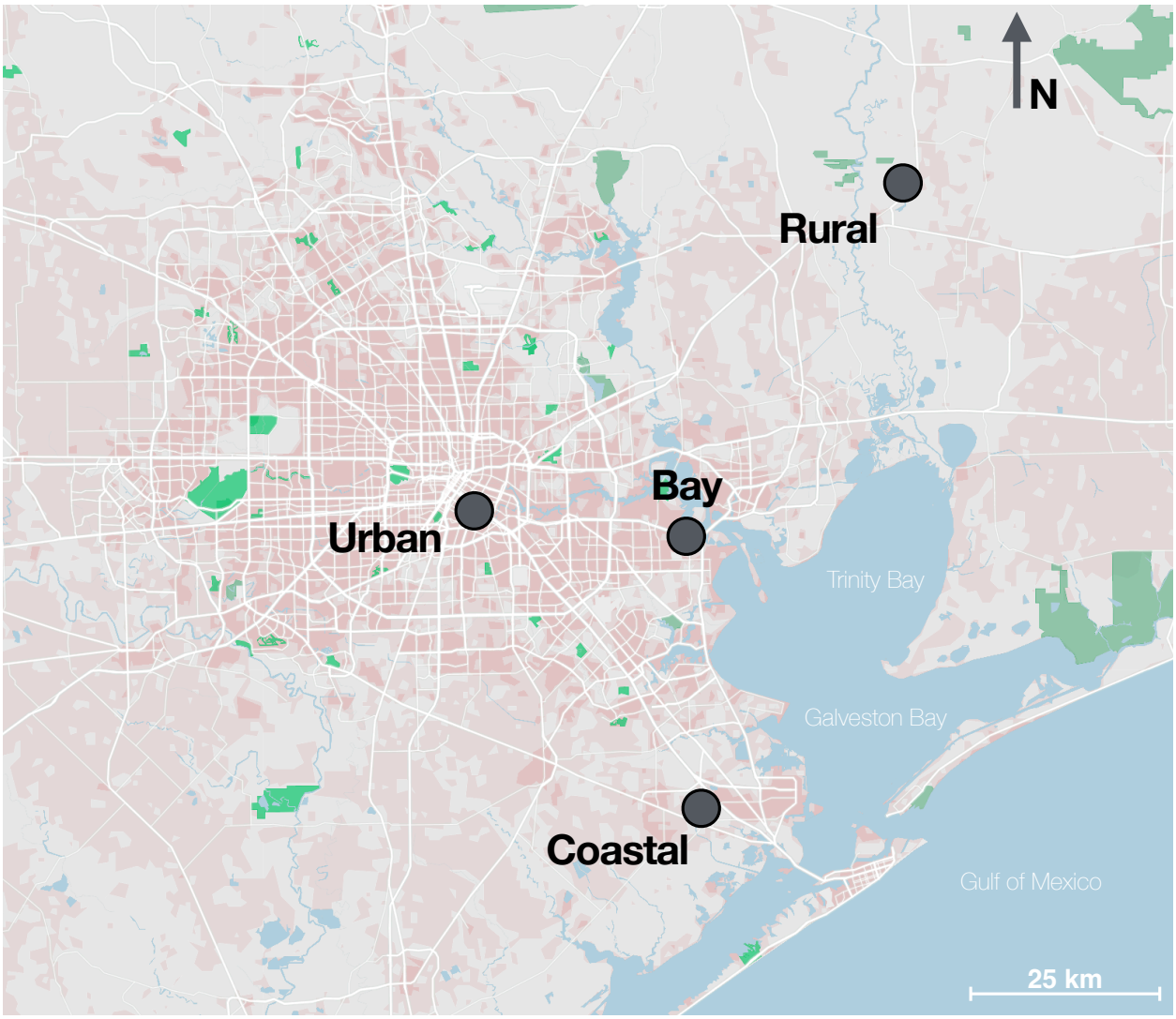

Figure 1: Location of the Urban, Bay, Coastal, and Rural field sites in the Houston Metropolitan area. Both the Coastal and Bay sites were heavily influenced by sea breeze. The Bay site was the primary TRACER site operated by the Department of Energy. The Urban site was located within the campus of University of Houston and located within the Inner Ring Road.

Convective systems entering the urban domain were observed using the S-Band Next Generation Weather Radar (NEXRAD) positioned at the KHGX location operated by the National Weather Service. When possible, the C-Band Scanning ARM Precipitation Radar, 2nd Generation (CSAPR2) provided additional observations. Both radars provided data on reflectivity (dBZ), doppler winds (ms^{-1}), differential reflectivity (dBZ), co-polar correlation coefficient (ρ_{HV}), and accumulated rain rate (mm/hr). NEXRAD radars have been shown to meet the high spatial resolution needs for urban observations (Mote et al., 2007). During active convection episodes, the CSAPR2 tracked travelling cloud cells from their initiation to dispersion (Bharadwaj et al., 2018). Radar data was imported to the Py-ART python library, which enabled data visualization and post-processing. Composite reflectivity data was obtained by collapsing the plan position indicator (PPI) reflectivity maxima across all sweeps onto a single plane (Helmus et al., 2016). This

provides more information on overall cloud structure within the domain than reflectivity from a single sweep (Rauber and Nesbitt, 2018).

2.2 Weather Research and Forecasting Model: During the CUBE campaign, an urbanized configuration of the Weather Research and Forecast model (WRF), version 4.2.2, was used to forecast daily meteorological conditions in the Houston Metropolitan area. This specific configuration integrates the Building Effect Parameterization and Building Energy Model (BEP-BEM) scheme, ensuring a more realistic representation of the city's urban landscape and enhancing the accuracy of our simulations and analyses. The model was configured using a two-way nested domain with horizontal resolutions of 3 km and 1 km, as depicted in Figure 2. The summary of physics parameterization is shown in Table 1. The model was run daily starting 1 June – 30 August 2022, with each simulation extending 48 hours into the future using the High-Resolution Rapid Refresh (HRRR) 6Z forecast product from the National Oceanic and Atmospheric Administration (NOAA) as the initial and boundary conditions which provides atmospheric and surface data fields at 3 km resolution for the contiguous United States. The model was set up with 51 vertical levels, with 15 of them situated within the lowest 3 km of the atmosphere to accurately resolve processes within the urban boundary layer. The highest resolution domain contained the Houston Metropolitan area. A time step of 54 seconds was used for the outer domain. The model physics included the NOAH land surface model, the Rapid Radiative Transfer Model for Global Circulation Models (RRTMG) for both longwave and shortwave radiation, the Mellor–Yamada–Nakanishi–Niino Eddy Diffusivity Mass-Flux boundary layer scheme, and the Aerosol aware Thompson microphysics scheme. This daily forecasting approach allowed us to accumulate a comprehensive dataset for the entire campaign period.

Assessing the physical processes within the Houston urban environment requires a detailed description of the complex urban structure. To achieve this, we used a standardized framework for classifying and describing urban and natural landscapes based on local climate zones (LCZs), as introduced by Stewart and Oke (2012). The LCZ data for Houston was obtained from a 100 m-resolution global map of LCZs. This map was generated by (Demuzere et al. 2022) and based of a comprehensive machine learning approach employing lightweight random forest models. The models were trained using an unprecedented volume of labeled training areas, alongside a vast array of earth observation images. This data was processed to align with the WRF model's grid system and subsequently integrated into the model. The LCZ information provides the basis for defining key urban parameters in the WRF model, such as building fraction, building density, and average building height. Model performance was evaluated against surface observations from the Automated Surface Observing System (ASOS) network. Evaluation metrics included root mean square error (RMSE), bias, and R^2. These statistics were used to compare the modeled surface temperatures with the observations at three urban stations: MCJ, IAH, DWH, and two rural stations: ARM, T78. Overall, the RMSE varied between 1.31 and 1.56; the R^2 values at all sites were higher than 0.85. The largest bias 0.37˚C and the lowest was -0.73˚C. The performance of the forecasts was in line with other studies in literature.

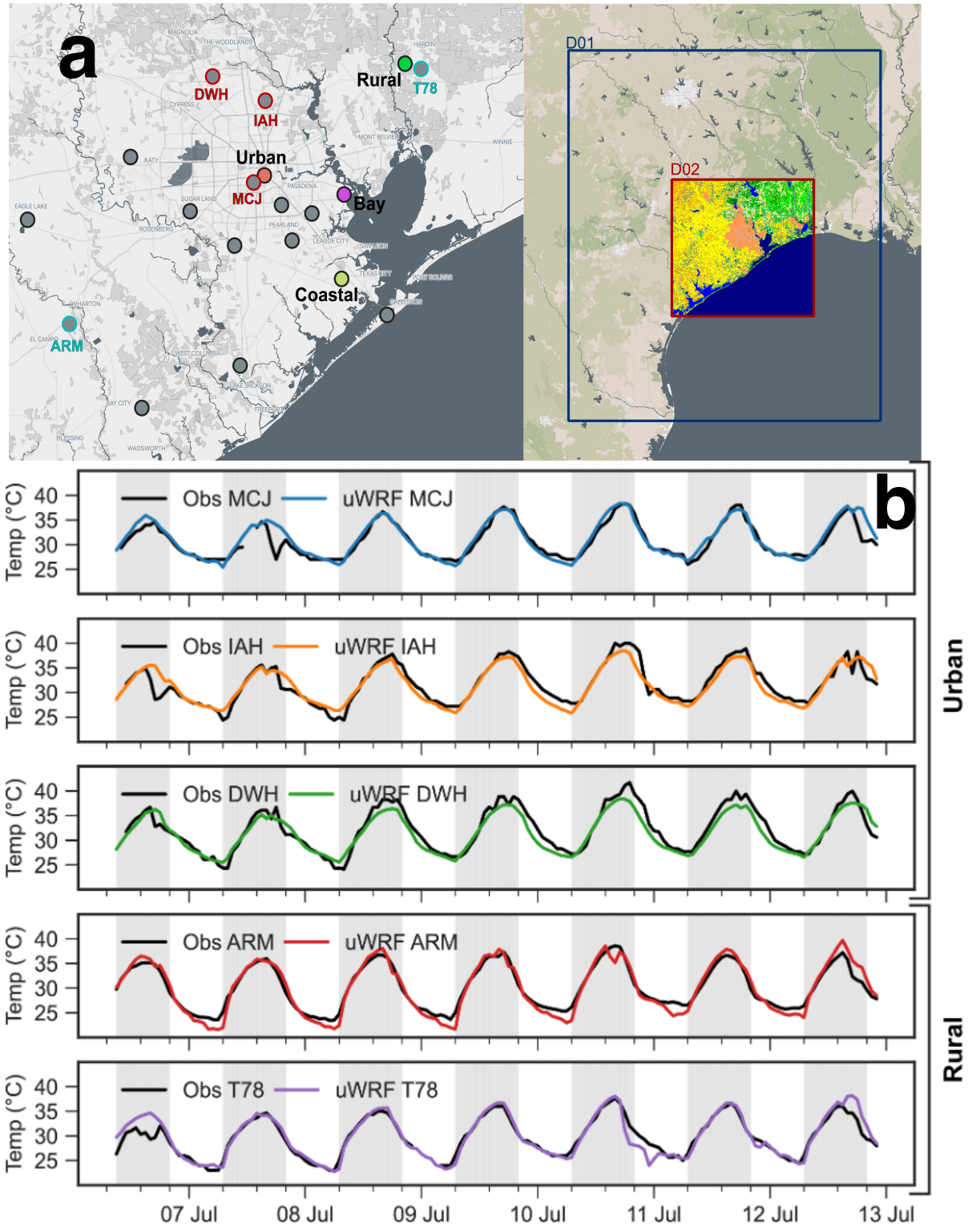

Figure 2: The top plot (a) shows the location of the observation sites along with the simulation domain; apart from Rural, Urban, Bay, and Coastal, all other sites were operated by the National Weather Service. The bottom plots (b) compare the simulations with the data observations at multiple sites. Overall, the model performed well in reproducing the 2-m temperature at multiple locations.

Table 1: Summary of physics parameterization.

Model Configuration	**Domain 1**	**Domain 2**
Horizontal grid points	258 x 302	352 x 334
Δx (km)	3	1
Vertical Layers	51	
Cumulus physics	None	
Longwave radiation	RRTMG	
Shortwave radiation	RRTMG	
Microphysics	Aerosol aware Thompson	
Planetary boundary layer physics	MYNN-EDMF	
Land surface physics	NOAH-LSM	
Urban physics	BEP + BEM	
Initial / boundary conditions	NOAA HRRR	

3.0 Results

Houston metropolitan and surrounding sub-urban areas located near Southeast Texas have a humid subtropical climate with sea breeze influence from the Gulf of Mexico during the summer season.

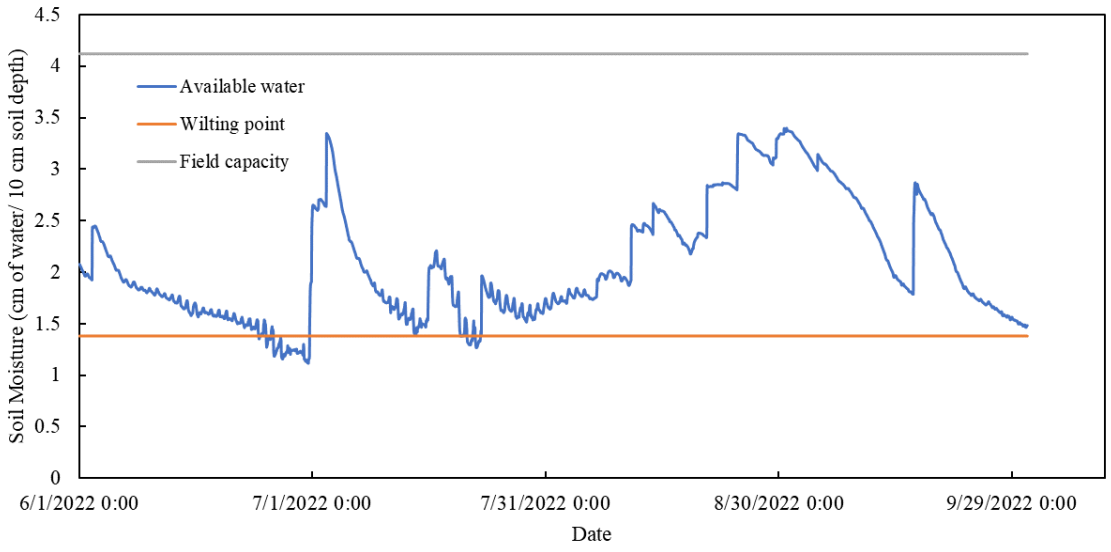

Figure 3: Soil moisture variability during the field campaign in the sub-urban site at LaPorte, TX. We compared the available water with the field capacity and permanent wilting point for the soil type in the sub-urban La Porte site to understand the soil moisture scenario at the field site. The La Porte site is located within the Harris County where the soil is mostly Lake Charles Clay within 11 inches depth as per the data from Web Soil Survey (National Cooperative Soil Survey) website. The data regarding field capacity and permanent wilting point for the clayey soil is obtained from the USDA Soil Survey Geographic Database (SSURGO) by the North American Land Data Assimilation System (NLDAS).

Houston has 3 months of hot, humid summer season from June through August, with August being the hottest month with an average high temperature of 94°F, and a record high of 109°F. In our study period, the weather in Houston and surrounding region was drier than normal due to the La Nina effect. A warmer summer than typical is also evident from the available soil moisture data collected at the Bay (La Porte) site, where a significant soil moisture deficit was observed during the June-July period (Figure 3). June 2022 was unusually drier than usual, causing severe drought conditions in Houston and the surrounding area. The monthly precipitation total for Houston was 3.3 mm, 34.3 mm, and 217.9 mm for June, July, and August, respectively; June and July were 149.1 mm and 61.5 mm below normal, while August was 95 mm above normal.

3.1 Surface-layer Characteristics

3.1.1 Mean meteorological characteristics: The diurnal temperatures for June and August 2022 are compared in Figure 4. Among the four sites, the urban site recorded the highest temperature, 38.3 °C on June 20 at 2130 UTC. In general, July was the hottest month of the year for all the sites. Among the four sites, the urban site experienced the highest temperatures, while the rural site experienced the lowest temperatures for all the months. Between the coastal and bay site, higher average temperatures were observed at the bay site.

The maximum half-hour average temperature in July was 35.77 °C between 20:30 and 21:00 UTC and the minimum was 29.89 °C (i.e., highest minimum of the months) between 11:30 and 12:00 UTC in the urban site. It is important to note that while averaging temperatures for the urban site, we considered 17 days in June and 23 days in July due to the unavailability of time series data for the remaining days. In the case of the coastal site at Galveston, the highest 30-minute average temperature in July was 34.84 °C, and the minimum was 27.58 °C, displaying a greater nocturnal temperature drop than the urban site. With a peak average daytime temperature of 34.83 °C and a lowest average nighttime temperature of 26.27 °C, the rural site experienced the largest nocturnal temperature declines among the sites in July. The higher temperature in urban environments are related to the lack of impermeable surfaces that are efficient in storing heat, leading to the urban heat island (UHI) effect. The maximum UHI (here calculated as the difference between the Urban and the Rural site) for June, July, and August were observed right before sunrise at 1100 UTC and were around 4.5 ˚C, 3.7 ˚C, and 3.6 ˚C, respectively. While not shown here, in September 2022, the maximum UHI was around 5.4 ˚C. It should be noted that the average UHI remains almost constant throughout the day. In many other cities, the nighttime UHI is much higher than the daytime. In New York City, another coastal urban environment, the UHI ranged between 3˚C during the nighttime to less than 0.5˚C during the convective period. The two coastal sites experienced the highest variability in diurnal temperatures; the daytime maximum at the LaPorte and Coastal sites matched that of the urban site; however, during the nighttime, the average temperatures were close to that of the rural site. The shift is primarily due to the relative lack of built surfaces at both coastal sites.

We also studied the diurnal temperature variations during the heat wave periods as defined by NWS, sea breeze days and non-sea breeze days. The characteristics of Urban Heat Island (UHI) are monitored during the heat wave periods (i.e., during June 11 through June 13, July 20 through July 21) during the field campaign. In general, UHI effect decreased during the heat wave episode

(6/11–6/13) compared to typical summer days, with UHI at the urban site decreasing to 0.94 °C in the morning between 12:00 to 12:30 UTC, and 3.75 °C in the afternoon between 23 and 23:30 UTC. For the heat wave during July 20 through July 21, UHI remained within 1.17 °C to 2.67 °C, with nearly identical UHI values in the morning and afternoon periods.

3.1.2 Surface layer turbulence characteristics: We computed turbulent kinetic energy (TKE) for all the sites during the field campaign utilizing instantaneous wind fluctuations from the flux measurements. As expected, high turbulent kinetic energy (TKE) was observed at the Urban site all through the day (Figure 5). The high TKE is primarily due to wind shear caused by high surface roughness (Srivastava and Sarthi, 2002). We noticed higher TKE peak values in June-July period than August-September. The TKE typically peaks between 20:00 and 20:30 UTC in June, 22:30 to 23:00 UTC in July, 22:00 to 22:30 UTC in August, and 18:30 to 19:00 UTC in September at the Urban site. Sea breeze contributes to high TKE at both Coastal and Bay site, with Bay station having slightly greater TKE than the Coastal, but lower than the urban location. Among the sites, the Rural site displayed the lowest TKE values diurnally, indicating less wind shear than the other sites (Figure 5). Urban, coastal, and rural sites showed much higher peak TKE values (nearly doubled for urban site) than the monthly average during heat wave occurrences (i.e., during June 11 through June 13, July 20 through July 21). Higher TKEs during both heat wave occurrences were mostly due to sea breeze-driven wind flows, which allowed maritime cool air to migrate to the land surface through temperature gradients formed as a result of the land surface and surrounding airmass heating (Cuxart et al., 2014). High TKE was observed even during nighttime hours, mostly due to onshore winds.

3.1.3 Surface Energy Fluxes: For each of the selected four locations in the Houston Metropolitan Area, we estimated the diurnal and monthly variation of sensible and latent heat fluxes. In general, for the months of June, July, and August, the urban site experienced higher half-hourly sensible heat flux than the latent heat flux (Figure 6). Furthermore, the peak 30-minute average value of the diurnal sensible and latent heat flux gradually decreased from June to August at the urban site

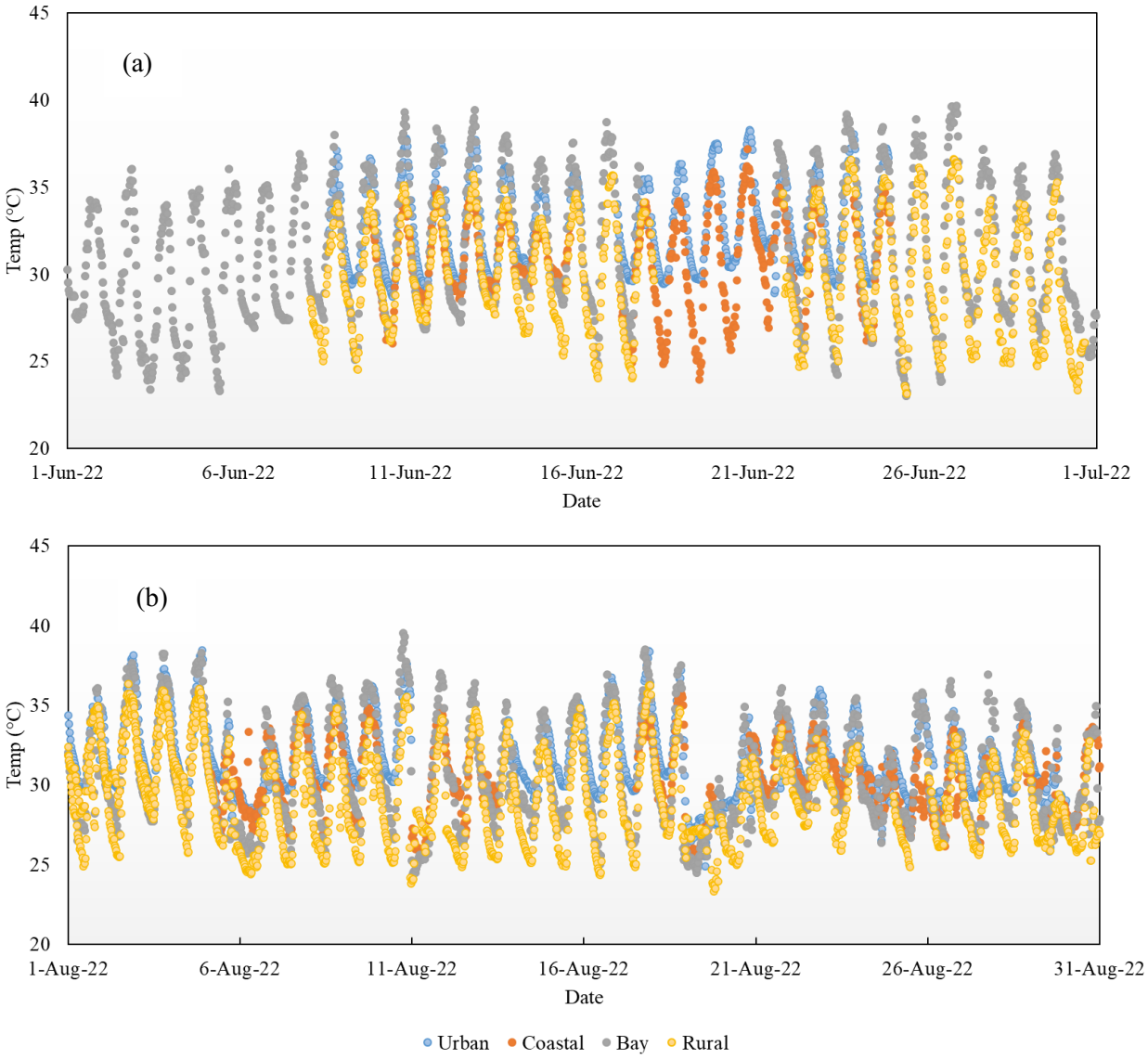

Figure 4. Diurnal temperature variation for the months of (a) June, and (b) August in the Urban, Bay, Coastal and Rural sites around the Houston area.

(Figure 6). The difference between the peak half-hourly sensible and latent heat flux was higher during the month of July compared to other months. Higher latent heat fluxes were observed during September due to increased precipitation. The time of the peak latent heat flux varied monthly; particularly, the peak for June was at 22:30 UTC, and for August was at 20:30 UTC. At the urban site, the Latent heat flux signal lacked a clear diurnal cycle; the lack of vegetation and permeable surfaces is primarily responsible for this effect. The sensible heat flux values at the urban site are comparable to those observed at other sites (Figure 6). The majority of the incoming

radiation is absorbed by the built surfaces, which then redistributes the heat as sensible heat flux throughout the day (Hrisko et al. 2021a).

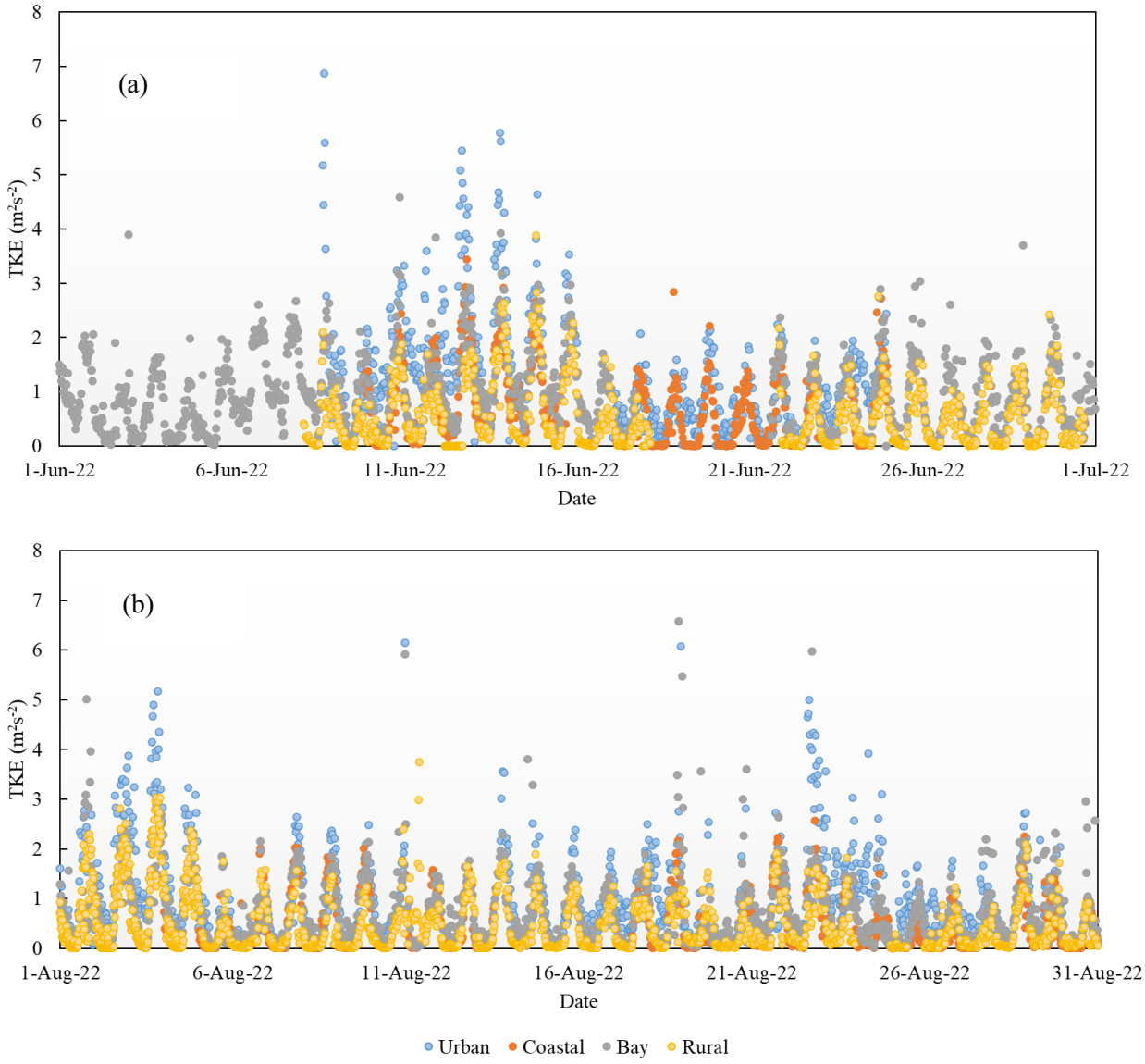

Figure 5. Diurnal turbulent kinetic energy variation for the months of (a) June, and (b) August in the Urban, Bay, Coastal and Rural sites around the Houston area. From June to September, we observed a progressive decline in the peaks of u for the Bay site.*

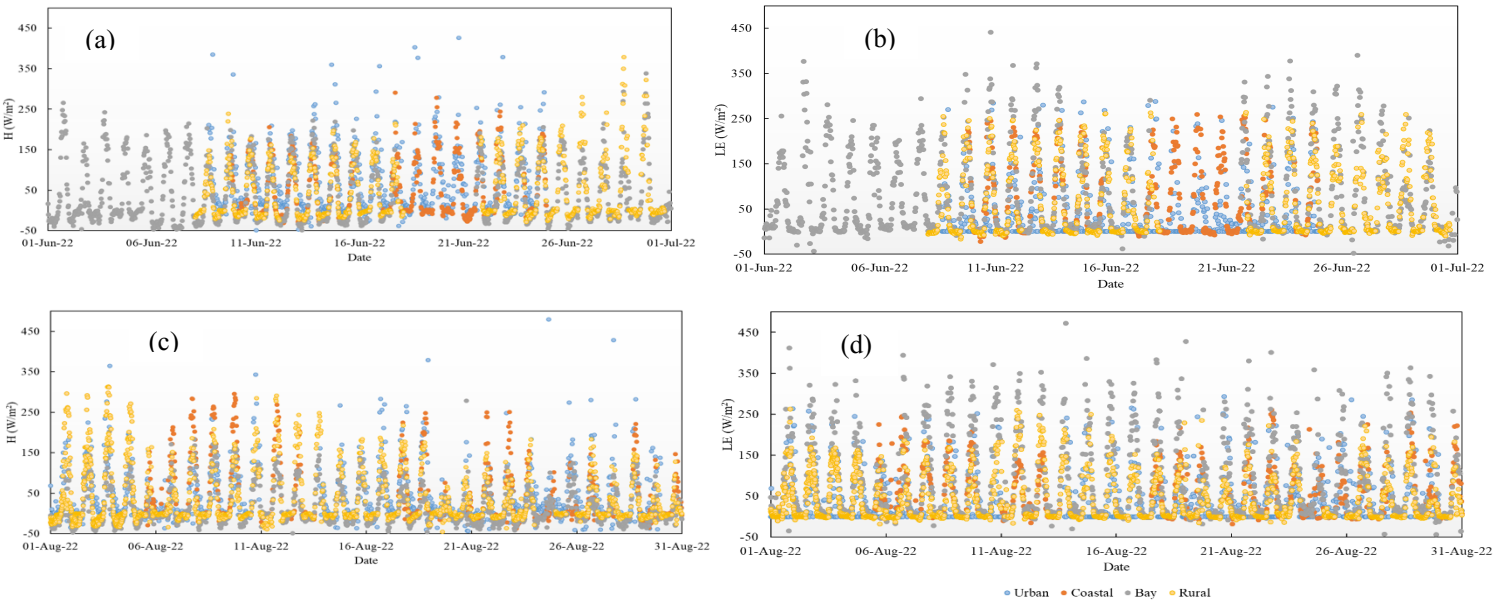

Figure 6 Diurnal sensible (H) and latent heat flux (LE) variation for the month of (a, b) June, and (c, d) August in the Urban, Bay, Coastal and Rural sites around the Houston area.

For the case of Coastal site, the peak half-hourly sensible heat flux was higher compared to the latent heat flux during the months of July and August (Figure 6). However, the latent heat flux was comparatively higher than the sensible heat flux during June indicating a shift of heat flux trend from June to July. In contrast, latent heat flux dominated over the sensible heat flux for all four months at the Bay site. The peak Bowen ratio at the coastal site is around 0.8, with high sensible and latent heat. Though the peak half-hourly average latent heat flux remained the same throughout the study period at the Bay site, sensible heat flux gradually decreased from June to September. The difference between the Coastal and Bay sites is related to the landcover characteristics. The bay site had more green cover compared to the coastal site. The Rural site demonstrated different patterns of sensible and latent heat fluxes at different months. For example, we noticed a higher peak latent heat flux than sensible heat flux in both June and August, while a lower peak latent heat flux than sensible heat flux in July. The Bowen ratio at the rural site was around 0.8 but the average peak values were lower than the coastal site. At the bay site, the peak Bowen ratio exceeded 1 for the months of June through September.

3.1.4 Spectral Characteristics

Figure 7 shows the power and co-spectrum for streamwise velocity (u), vertical velocity (w), and vertical heat flux (w't'); both the power spectrum and the co-spectrum were computed for multiple 5-minute periods and averaged to obtain a smoother curve; only convective periods when the $z/L < 0$ (where z is the height of the measurement and L is the Monin-Obukhov length scale) were chosen. The power spectrum was normalized by friction velocity, and the co-spectrum was normalized by the corresponding flux. The frequency was normalized by the ratio of measurement height and the mean velocity to be consistent with other studies.

The power spectrum for the streamwise velocity (u) exhibits a strong variation in both normalized peak frequency and normalized energy density across the coastal-rural-urban transect. The rural site peaks near 0.01, almost a factor of ten behind the urban site, around 0.1. The coastal site peaks

at around 0.05. While the coastal and the rural sites have a hump-back shape and a distinct peak, the urban site has a plateau, with high contributions at multiple frequencies. This behavior is consistent with previous urban studies. The difference in peak frequency suggests that the coastal and urban sites were more impacted by local flow regimes compared to the rural site. The difference in spectral energy density between the sites is related to higher u* values at urban and coastal sites, where the turbulent length scale is equivalent to the mean velocity scale.

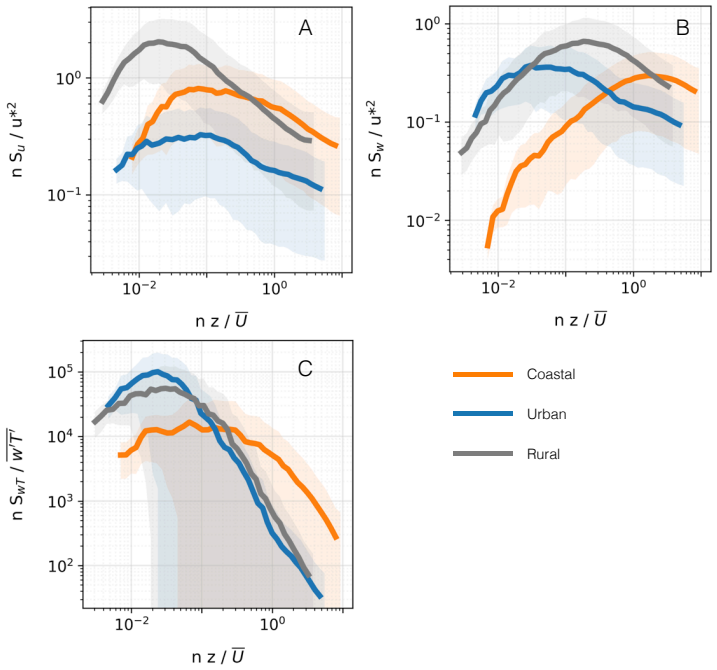

Figure 7: Power spectra and cospectra of streamwise velocity, vertical velocity, and vertical heat flux. All spectra are pre-multiplied and plotted against non-dimensional frequency where n denotes frequency, z denotes height above ground level, and U‾

In stark contrast, the power spectrum for w show a lower normalized peak frequency for the urban site, around 0.03; the rural site is a factor of ten behind, around 0.2, and the coastal site peaks at 2. Increased roughness and high convection are primarily responsible for the lower peak frequency observed at the urban site. Similarly, the w't' cospectra shows relatively lower normalized peak frequency for the urban site, followed by the rural and coastal sites. The coastal site exhibits a flat profile compared to the urban and coastal sites, which have a distinct peak frequency and a traditional hump shape.

Overall, the spectral analysis exhibits the presence of vastly different flow regimes along the coastal-rural-urban transect. The coastal site is dominated by the sea breeze effect that dictates the transport of heat and momentum. The urban and rural sites are influenced by local land cover characteristics that impact the hygro-thermal climate.

3.2 Boundary-layer Characteristics

The cloud top height was measured using the Ceilometer at the urban, rural, and bay sites. Figure 8 shows the maximum height each day over the summer. At the urban area, the maximum boundary layer height exceeded 3 km on most days; the average maximum height for June, July, and August was 3060 m. At the rural site, the values were above 2500 m on most days, with the average maximum being 2684 m. Both the urban and rural sites had fairly consistent values throughout the summer with similar mean and median values. At the bay site, the maximum boundary layer height was less consistent; on most days, they ranged above 2500 m. However, the values dropped below 2,000 m on several days. The difference in boundary layer height between the urban site and the rest two is mostly related to increased convection in urban areas due to anthropogenic modification of land cover and waste heat from air conditioning use. The lower boundary layer height observed at the Bay site is most probably related to low-level clouds and a lower Bowen Ratio.

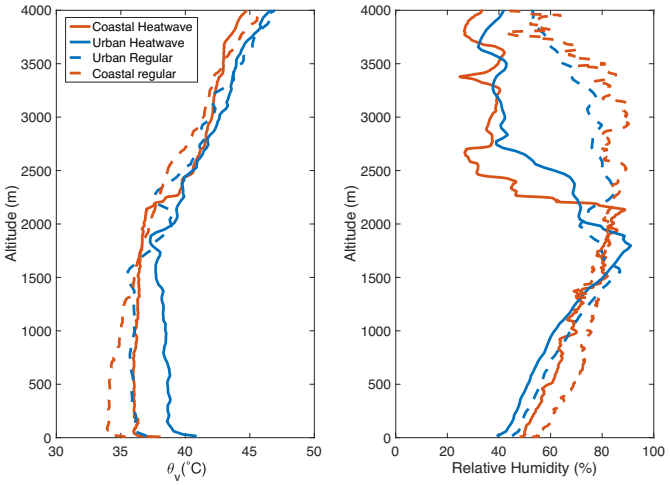

Figure 8: Profiles of virtual potential temperature and relative humidity at the urban and coastal sites for heatwave and regular periods.

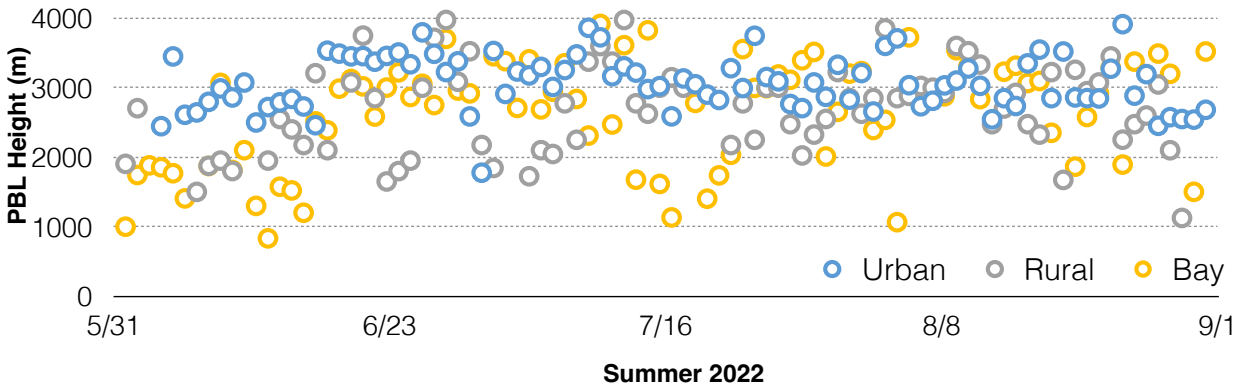

Figure 9: Daily maximum boundary layer heights at Urban, Rural, and Bay sites. The observations were made using a Ceilometer.

Error! Reference source not found. shows the boundary layer profiles of virtual potential temperature and relative humidity for the Coastal and Urban sites for 2 different time periods: a normal day and a heatwave day. Both the soundings were recorded during the afternoon convective period. While many radiosondes were launched during the campaign, we picked these periods as they were representative of typical convective periods observed in the Houston Metropolitan area. The boundary layer height during a typical convective period was close to 1500 m, however during heatwave episodes they peaked above 2000 m, nearly 33% deeper. On a normal day, the urban boundary layer was around 2˚C warmer than the coastal environment; the difference gradually weakened with height, achieving parity at the height of the boundary layer. During the heatwave periods the urban site was around 3˚C warmer than the coastal site and remained on average 2˚C warmer in the lower 1500 m. The amplification in boundary layer temperature at the urban site during the heatwave period was more pronounced compared to the coastal site; for example, at 1000 m above ground level, the urban site was around 2.5˚C warmer compared to 1.1˚C at the coastal site.

The relative humidity profile predictably shows a drier atmosphere at the urban site relative to the coastal site; the relative humidity at the coastal site was on average 10% higher (Figure 9). The difference in relative humidity between the regular and heatwave day at the urban and coastal sites remained unchanged. During the heatwave episode the lower troposphere (above the boundary layer) was significantly drier. At both the urban and coastal sites, the relative humidity values dipped below 50%. However, during the non-heatwave period, the values above the boundary layer were between 60-80%. The lower values could be related to the subsidence of dry air mass from upper troposphere during the heatwave episodes.

The results show how heatwave episodes impact not just the near-surface temperature but the entire boundary layer. Further, urbanization plays a significant role in amplifying the thermal state of the boundary layer.

3.2.1 Spatial Variability in Boundary-layer Characteristics

To study spatial variability, we rely on urban WRF simulations. Figure 10a and 10b show the variability in 2m air temperature, 10m wind, and the planetary boundary layer (PBL) height for a typical summer afternoon on July 10th, 2022. Figures 10c and 10d show the variability in PBL height (purple line) and potential temperature contours along two cross sections: cross section AA which runs from southeast to northwest and cross section BB, which runs from northeast to southwest. Plot C also shows the variability in wind speed and direction with height. The day and time period was typical of a normal convective period in Houston.

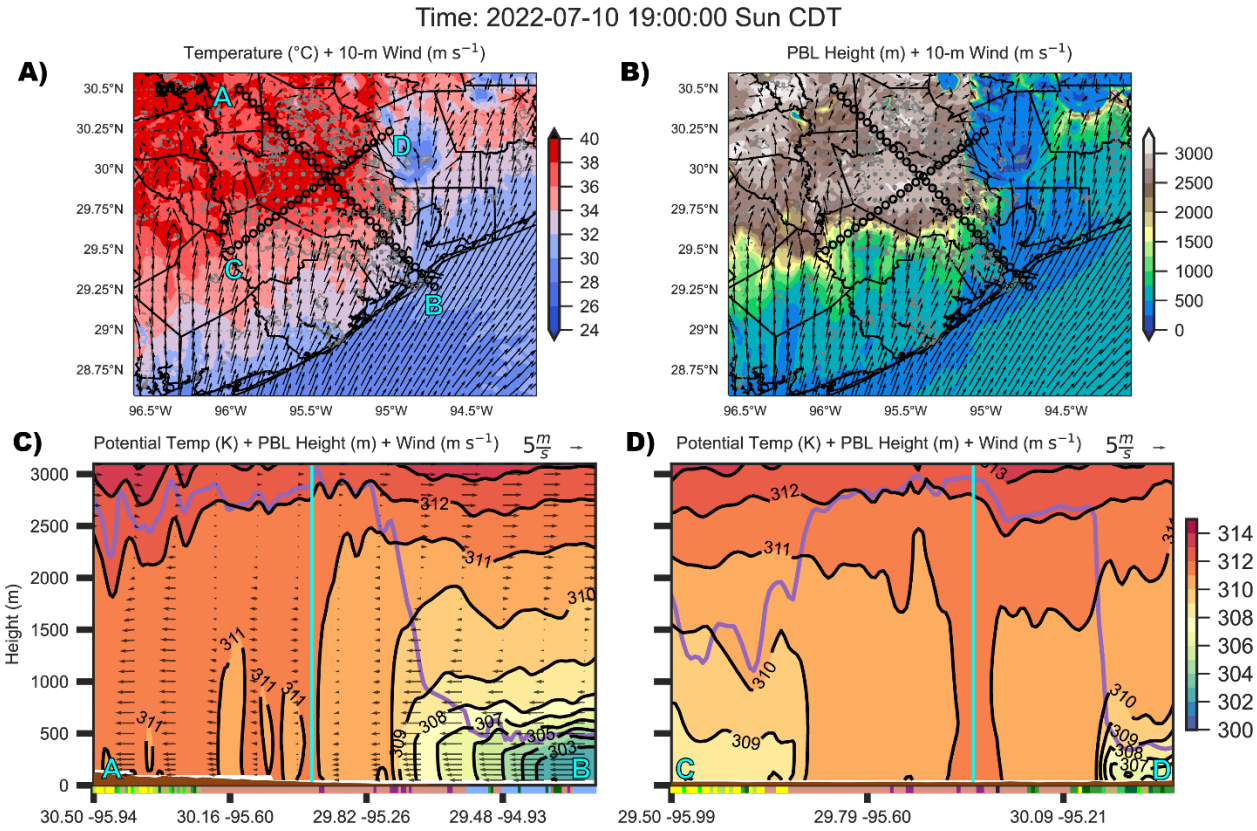

Figure 10: All 4 plots describe the spatial variability in boundary layer characteristics. (A) Plot A shows the variability in 2-m temperature and wind field; (B) plot B shows the variability in boundary layer height; plots C and D show variability in potential

temperature and boundary layer height along (C) east-west and (D) north-south. The results were obtained from the urban WRF simulation for a typical summer day during the convective period (July 10th 2022).

Figure 10a captures the air temperature gradient; the regions closer to the coastline are 4-5˚C cooler than the urban domain; the maximum air temperature reaches above 38˚C. Similar to the thermal gradient, there is a high variability in wind speed; the region close to the coast experience significantly higher wind speeds compared to the urban core. Moreover, the wind direction within the urban core is highly inconsistent. While the temperature difference is due to change in the partitioning of the surface energy budget, the change in wind characteristics is related to increased aerodynamic drag and thermally gradient.

The boundary layer is much deeper in the urban core; Figure 10b shows the PBL height within the urban core to be around 2000 m - 2500 m, while in the non-urbanized coastal regions, it is between 1000 m - 1500 m. This is consistent with observations from the ceilometer, where the average mixed layer height was over 2000 m at the urban site. Figure 10c shows how the PBL height varies across the urban-coastal interface. Close to the water, the PBL height is close to 500 m, and does not vary much inland. Once the land becomes urbanized, the PBL depth increases dramatically. PBL height holds around 2500 m throughout the entire urban core. The figure captures the reduction in wind speed throughout the PBL; the near-surface winds close to the coast are between 5-10 ms^{-1}, and the urban domain winds are 1-2 ms^{-1}. The sea breeze circulation is evident; the winds below 1000 m are south easterlies while the winds above 1000 m are northwesterly.

3.3 Impact of sea breeze on UHI

Microscale impacts of the Houston urban environment culminate within mesoscale phenomena. Surface observations of 2 m temperature from both ASOS and Synoptic Data weather stations are interpolated and overlaid with 10m wind barb vectors, where the left and right columns of Figure 11 illustrate the pre- and post-SBF surface conditions, respectively, for 12 July - the highest heat index day during the CUBE campaign. The pre-SBF conditions at 1330 LT (Fig. 11a), when the front is initially on land, show no distinct UHI due to elevated rural temperatures extending north of the city. This is typically associated with enhanced solar heating rates in rural areas (Oke et al., 2017). The SBF follows the shape of coastal irregularities such as the Bay, which brings cooler temperatures further onshore to its east. Despite the lack of clear UHI, the onshore temperature gradient is strongest across the city. Winds behind the front are south easterly near the Bay and easterly (along shore) to the west of the city. Precipitation ahead of the SBF for the hour before 14 LT (Fig. 11c) shows isolated and widespread convective initiation outside of Houston.

After the SBF has passed much of the city at 1630 LT (Fig. 11b), a strong UHI to the east (upwind) of the city developed. The UHI region is warmer than it was at 1330 LT. The SBF convergence is heavily bowed southward and follows the eastern extent of the city. This bowed convergence is due to the building effect (Gaffen & Bornstein, 1988; Han et al., 2022), which modified onshore movement of cool marine air and separated it from the warm urban air. Temperatures are coldest in regions extending westward (downwind) from the city, which induces a city scale temperature gradient that is oriented perpendicular (east-west) to the expected coastal scale temperature gradient (north-south). Faster winds behind the SBF converge west of the city and further

downwind, while weaker winds converge into the UHI and bowed SBF on the east (upwind) half. For the hour preceding 17 LT (Fig. 11d), the radar shows accumulated precipitation is reduced to the east (upwind) and enhanced to the west (downwind) of the city due to the modification of regional winds. The city along the front remained dry. The regions with the strongest winds are associated with the precipitation maxima, likely to be due to convection enhanced by downwind urban reconvergence and SBF flow.

The results for an isolated convection case illustrated that Houston modified precipitation not through the expected bifurcation or initiation mechanisms (Dou et al., 2015), but instead primarily by alteration of the SBF. The pre-SBF environment showed little urban influence on precipitation, while a canonical downwind enhancement pattern developed post-SBF. Rather than eliminate the UHI, the SBF developed it due to the building effect, which stalled progression of the front into urban regions and prolonged diurnal heating in pre-SBF areas.

4.0 Discussion

The results show the unique boundary layer characteristics along the coastal-urban-rural gradient. As expected, the near-surface air temperature at the urban site is higher than the other three sites throughout the day. The difference in the temperature is highest during the nighttime period when the urban materials redistribute the stored heat as sensible heat. At midnight, a 2.5 ˚C - 3 ˚C difference is observed between the urban and the non-urban sites. While the rural temperature decreases rapidly during the nighttime period, the temperature at the coastal, bay, and urban sites decreases more slowly. At the bay and the coastal sites, the localized land breezes may be responsible for the reduced rate. The bay site, situated in a residential neighborhood, experiences maximum diurnal variability; the near-surface air temperature is as high as the urban site during the afternoon and as low as the rural site during the midnight hour. This unique behavior is also observed in the TKE variability; the Urban site, as expected, has the highest TKE values throughout the day. The tall and uneven roughness that dominates the urban landscape is primarily responsible for the high TKE values. The rural site records relatively lower values throughout the day. The TKE values at the coastal and bay sites fall in between the other two sites. During the daytime period, the high TKE values at the coastal and the bay sites are due to strong thermally driven winds.

During the dry period in June, the sensible heat flux during the daytime period was identical at all 4 sites. However, during the nighttime period, the fluxes at the urban site were positive, with values between 5 - 50 Wm^{-2}. At the other 3 sites, the fluxes were negative during the nighttime period. The high sensible heat flux at the urban site is primarily responsible for the high urban heat island intensity observed during the nighttime hours. The latent heat flux values were similar during June at the coastal, bay, and rural sites; however, at the urban site, the values were notably lower. The low values at the urban site are due to lack of vegetation or bare soil. At all 3 non-urban sites, the Bowen Ratio during June was close to 1. In August, when the soil was wetter than normal, the sensible heat flux at all the sites was comparatively low. It should be noted that while the sensible heat flux dominates at the urban site, the values are identical to other sites. In urban areas, the net radiation is partitioned between sensible, storage, and latent heat fluxes. However, at the non-urban sites, the balance is between sensible and latent heat fluxes. While the storage heat fluxes were not

observed in Houston, past research has shown values as high as 200 Wm^{-2} (Hrisko et al. 2020, Hrisko et al. 2021a, Hrisko et al. 2021b) in dense urban environments.

The most striking difference between the sites is observed in the power and co-spectra of zonal and vertical velocities and the vertical heat flux. The dominant frequencies observed at the coastal site are very high compared to the other two. For the vertical velocity power spectra, the non-dimensional peak frequency at the coastal site is a factor of ten above the rural site and twice the factor of ten above the urban site. For the zonal velocity, the peak frequency at the coastal site is half a factor of ten above the two sites. The results show that the turbulence in the coastal site is highly influenced by local factors: thermally driven sea/land breezes are mostly responsible for the turbulent transport of momentum and heat. At the urban and rural sites, where the peak frequencies are in line with previous studies (Collier 2006, Fu et al. 2008, Li and Liu 2022), the local landcover characteristics dictate the transport. Additionally, at the urban site, the storage heat flux plays a dominant role; the total surface energy fluxes (sum of sensible and latent heat) at the urban site are much lower compared to the rural site. While some of the differences are related to advection, the urban land cover stores more heat: concrete has a very high thermal capacity.

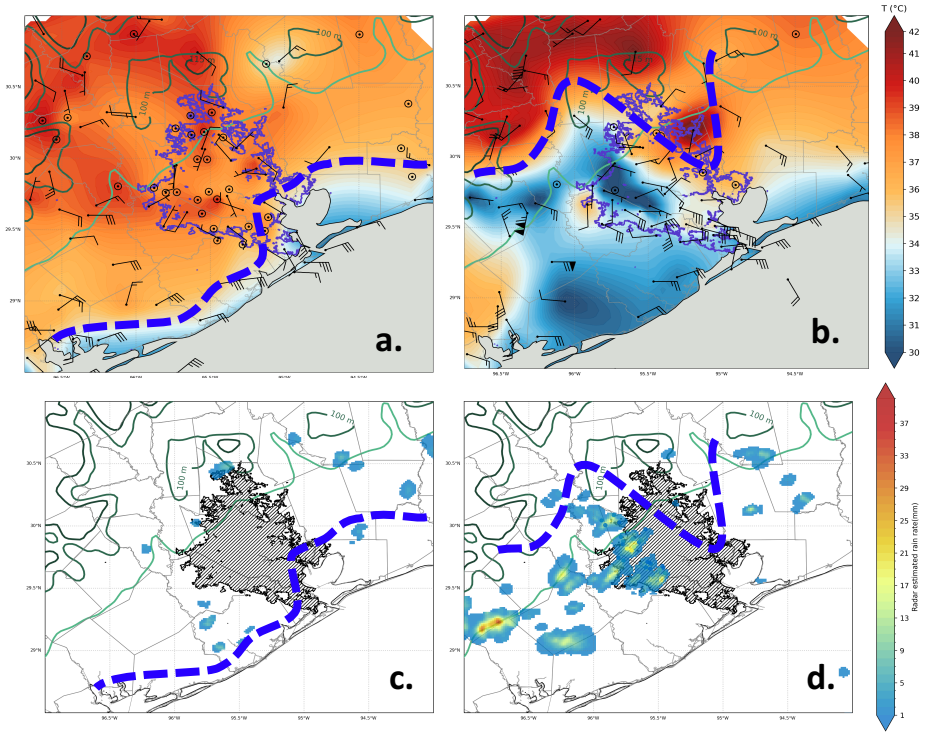

Figure 11 shows the movement of the sea breeze front at (a) 1330 LT and (b) 1630 LT on July 12, 2022, and its impacts on 2-m temperature, surface winds, and accumulated precipitation for the hour before (c) 14 LT, and (d) 16 LT. Data from surface observation stations and NEXRAD radar were used in this plot.

5.0 Conclusion

The paper analyzed the unique boundary layer characteristics along the coastal-urban-rural gradient. Coastal urban environments are influenced by the interaction between the urban heat

island phenomenon and the sea breeze effect. Here, we used both ground-based micrometeorological observations and an urban climate model to highlight the mean and turbulence characteristics.

Our results show that the surface energy fluxes were highly variable across the sites. While the peak sensible heat fluxes were similar in all four measurement sites, the latent heat flux at the urban site was lower. Additionally, during the early summer dry periods, the Bowen Ratio was higher than 1 in the rural site, and during the wetter months, the peak Bowen Ratio at the rural site was less than 1. The urban site, however, exhibited no such seasonal variability. At the Coastal and Bay sites, the latent heat fluxes dominated.

The turbulent kinetic energy was high at the urban, Coastal, and Bay sites compared to the rural environment. The thermally driven winds at the Coastal and Bay sites were primarily responsible for the high TKE. The local winds also play a significant role in the transport of momentum and heat; at the coastal site the dominant turbulent length scales were much lower compared to the urban and rural areas.

As expected, the average boundary layer height at the urban site was much higher compared to the non-urban ones. Modeled results showed a sudden jump in boundary layer height as we traversed from the coast to the urban area. Radiosonde data during normal and heatwave episodes showed amplification in the air temperature throughout the boundary layer; however, the amplification was higher at the urban site. Finally, the urban landcover significantly influenced the development of the sea breeze front.

Future efforts will focus on furthering scientific understanding of urban thermal & mechanical processes as they relate to SBFs, deep convection, and precipitation modification. The three main paths this will be accomplished by is investigating a.) the mesoscale interactions between coastal, topographic, and urban areas under various synoptic conditions, b.) the balance between urban dynamics and aerosols, c.) the evolution of urban processes during precipitation, and their role in precipitation modification.

Acknowledgment

The authors would like to thank Dr. Michael Jensen and his TRACER team. The observational data can be accessed at https://cube.omaraddasi.com.

Funding

The work was funded by US NSF Geo 1802226. NOAA NA16SEC4810008 supported some students who worked on the project.

Competing interest declaration

There are competing interests to declare.

References

Atmospheric Radiation Measurement (ARM) user facility. 2021. Ceilometer (CEIL10M). 2022-06-01 to 2022-09-30, ARM Mobile Facility (HOU) Houston, TX; AMF1 (main site for TRACER) (M1). Compiled by V. Morris and B. Ermold. ARM Data Center. Data set accessed 2022-11-27 at http://dx.doi.org/10.5439/1497398.

Atmospheric Radiation Measurement (ARM) user facility. 2021. Balloon-Borne Sounding System (SONDEWNPN). 2022-06-10 to 2022-09-30, ARM Mobile Facility (HOU) Houston, TX; AMF1 (main site for TRACER) (M1). Compiled by K. Burk. ARM Data Center. Data set accessed 2023-02-10 at http://dx.doi.org/10.5439/1595321.

Atmospheric Radiation Measurement (ARM) user facility. 2021. Eddy Correlation Flux Measurement System (30ECOR). 2022-06-01 to 2022-09-30, ARM Mobile Facility (HOU) Houston, TX; AMF1 (main site for TRACER) (M1). Compiled by R. Sullivan, D. Billesbach, E. Keeler and B. Ermold. ARM Data Center. Data set accessed 2022-11-16 at http://dx.doi.org/10.5439/1025039.

Atmospheric Radiation Measurement (ARM) user facility. 2021. Surface Energy Balance System (SEBS). 2022-06-01 to 2022-09-30, ARM Mobile Facility (HOU) Houston, TX; AMF1 (main site for TRACER) (M1). Compiled by R. Sullivan and E. Keeler. ARM Data Center. Data set accessed 2022-11-27 at http://dx.doi.org/10.5439/1025274.

R.M. Banta, C.J. Senff, T.B. Ryerson, J.W. Nielsen-Gammon, L.S. Darby, R.J. Alvarez, S.P. Sandberg, E.J. Williams, M. Trainer. A bad air day in Houston, *Bull. Am. Meteorol. Soc*., 86 (2005), pp. 657-669.

Bauer, T. J. 2020, Interaction of urban heat island effects and land–sea breezes during a New York City Heat Event, *J. Appl. Meteorol. Climatol*. Am. Meteorol. Soc., 59, 477-495, 10.1175/jamc-d-19-0061.1

Barlow, J. F. (2014). Progress in observing and modelling the urban boundary layer. *Urban Climate*, *10*, 216-240.

Bharadwaj, N., Collis, S., Hardin, J., Isom, B., Lindenmaier, I., Matthews, A., & Nelson, D. (2018), C-Band Scanning ARM Precipitation Radar (CSAPR2CFR). Atmospheric Radiation Measurement (ARM) User Facility. https://doi.org/10.5439/1467901

Caicedo, V., Rappenglueck, B., Cuchiara, G., Flynn, J., Ferrare, R., Scarino, A. J., Berkoff, T., Senff, C., Langford, A., and Lefer, B., (2019), Bay Breeze and Sea Breeze Circulation Impacts on the Planetary Boundary Layer and Air Quality from an Observed and Modeled DISCOVER-AQ Texas Case Study, J. Geophys. Res.-Atmos., 124, 7359–7378, https://doi.org/10.1029/2019jd030523.

Casadio, S., Di Sarra, A., Fiocco, G. et al. (1996) Convective characteristics of the nocturnal urban boundary layer as observed with Doppler sodar and Raman lidar. Boundary-Layer Meteorol 79, 375–391 (1996). https://doi.org/10.1007/BF00119405

Collier, C. G. (2006). The impact of urban areas on weather. *Quarterly Journal of the Royal Meteorological Society*, *132*(614), 1-25.

Chen, F., S. Miao, M. Tewari, J.-W. Bao, and H. Kusaka (2011), A numerical study of interactions between surface forcing and sea breeze circulations and their effects on stagnation in the greater Houston area, J. Geophys. Res., 116, D12105, doi:10.1029/2010JD015533.

Childs, P.P., Raman, S., 2005, Observations and numerical simulations of urban Heat Island and sea breeze circulations over New York City, *Pure Appl. Geophys*. Springer, 162, 1955-1980, 10.1007/s00024-005-2700-0

Cook DR and RC Sullivan. 2020. Eddy Correlation Flux Measurement System (ECOR) Instrument Handbook. Ed. by Robert Stafford, ARM user facility. DOE/SC-ARM/TR-052. 10.2172/1467448.

Cuxart, J., Jiménez, M. A., Telišman Prtenjak, M., & Grisogono, B. (2014). Study of a sea-breeze case through momentum, temperature, and turbulence budgets. *Journal of Applied Meteorology and Climatology*, *53*(11), 2589-2609.

Day, B. M., Rappenglück, B., Clements, C. B., Tucker, S. C., Brewer, W. A., (2010), Nocturnal boundary layer characteristics and land breeze development in Houston, Texas during TexAQS II. Atmos Environ 44:4014–4023. https://doi.org/10.1016/j.atmosenv.2009.01.031

De Tomasi, F., Miglietta, M.M. & Perrone, M.R. (2011), The Growth of the Planetary Boundary Layer at a Coastal Site: a Case Study. *Boundary-Layer Meteorol* **139**, 521–541. https://doi.org/10.1007/s10546-011-9592-6

Demuzere, M., Kittner, J., Martilli, A., Mills, G., Moede, C., Stewart, I. D., ... & Bechtel, B. (2022). A global map of Local Climate Zones to support earth system modelling and urban scale environmental science. *Earth System Science Data Discussions*, *2022*, 1-57.

Dou, J., Wang, Y., Bornstein, R., & Miao, S. (2015). Observed Spatial Characteristics of Beijing Urban Climate Impacts on Summer Thunderstorms. *Journal of Applied Meteorology and Climatology*, *54*(1), 94–105. https://doi.org/10.1175/JAMC-D-13-0355.1

Emeis, S, K Schäfer, and C Münkel. 2009. “Observation of the structure of the urban boundary layer with different ceilometers and validation by RASS data.” Meteorologische Zeitschrift 18: 149–154.

Fan J, Rosenfeld D, Zhang Y, Giangrande SE, Li Z, Machado LAT, Martin ST, Yang Y, Wang J, Artaxo P, Barbosa HMJ, Braga RC, Comstock JM, Feng Z, Gao W, Gomes HB, Mei F, Pöhlker C, Pöhlker ML, Pöschl U, de Souza RAF. (2018), Substantial convection and precipitation enhancements by ultrafine aerosol particles. *Science*. 26;359(6374):411-418. doi: 10.1126/science.aan8461. PMID: 29371462.

Fan, J., Zhang, Y., Li, Z., Hu, J., & Rosenfeld, D. (2020). Urbanization-induced land and aerosol impacts on sea-breeze circulation and convective precipitation. *Atmospheric Chemistry and Physics*, *20*(22), 14163-14182.

Feng, K., Ouyang, M. & Lin, N. Tropical cyclone-blackout-heatwave compound hazard resilience in a changing climate. *Nat Commun* **13**, 4421 (2022). https://doi.org/10.1038/s41467-022-32018-4

Fu, J. Y., Li, Q. S., Wu, J. R., Xiao, Y. Q., & Song, L. L. (2008). Field measurements of boundary layer wind characteristics and wind-induced responses of super-tall buildings. *Journal of Wind Engineering and Industrial Aerodynamics*, *96*(8-9), 1332-1358.

Gaffen, D., & Bornstein, R. D. (1988). Case study of urban interactions with a synoptic scale cold front. *Meteorology and Atmospheric Physics*, *38*(4), 185–194. https://doi.org/10.1007/BF01054571

Gonzalez-Trevizo, M. E., Martinez-Torres, K. E., Armendariz-Lopez, J. F., Santamouris, M., Bojorquez-Morales, G., & Luna-Leon, A. (2021). Research trends on environmental, energy and vulnerability impacts of Urban Heat Islands: An overview. *Energy and Buildings*, *246*, 111051.

Goyal, M.K., Singh, S. & Jain, V. (2023). Heat waves characteristics intensification across Indian smart cities. *Sci Rep* **13**, 14786 (2023). https://doi.org/10.1038/s41598-023-41968-8.

Grotjahn, R., Black, R., Leung, R., Wehner, M. F., Barlow, M., Bosilovich, M., ... & Prabhat. (2016). North American extreme temperature events and related large scale meteorological patterns: a review of statistical methods, dynamics, modeling, and trends. *Climate Dynamics*, *46*, 1151-1184.

Han, Z. S., González-Cruz, J. E., Liu, H. N., Melecio-Vázquez, D., Gamarro, H., Wu, Y. H., Moshary, F., & Bornstein, R. (2022). Observed sea breeze life cycle in and around NYC: Impacts on UHI and ozone patterns. *Urban Climate*, *42*, 101109. https://doi.org/10.1016/j.uclim.2022.101109

Haman, C. L., B. L. Lefer, and G. A. Morris (2012), Seasonal variability in the diurnal evolution of the boundary layer in a near-coastal urban environment, *J. Atmos. Oceanic Technol.*, **29**(5), 697–710.

Helmus, J.J. & Collis, S.M., (2016). The Python ARM Radar Toolkit (Py-ART), a Library for Working with Weather Radar Data in the Python Programming Language. Journal of Open Research Software. 4(1), p.e25. DOI: http://doi.org/10.5334/jors.119

Hrisko, J., Ramamurthy, P., Gonzalez, J. E., (2021a) Estimating heat storage in urban areas using multispectral satellite data and machine learning, *Remote Sensing of Environment*, 252, https://doi.org/10.1016/j.rse.2020.112125.

Hrisko, J.; Ramamurthy, P.; Melecio-Vázquez, D.; Gonzalez, J.E. (2021b) Spatiotemporal Variability of Heat Storage in Major U.S. Cities—A Satellite-Based Analysis. *Remote Sens.*, *13*, 59. https://doi.org/10.3390/rs13010059

Hrisko, J., Ramamurthy, P., Yu, Y., Peng Yu, P., Melecio-Vázquez, D., 2020, Urban air temperature model using GOES-16 LST and a diurnal regressive neural network algorithm, Remote Sensing of Environment, 237, https://doi.org/10.1016/j.rse.2019.111495.

IPCC, 2014: Climate Change 2014: Synthesis Report. Contribution of Working Groups I, II and III to the Fifth Assessment Report of the Intergovernmental Panel on Climate Change [Core Writing Team, R.K. Pachauri and L.A. Meyer (eds.)]. IPCC, Geneva, Switzerland, 151 pp.

Liu, H., Zou, L., Xia, J., Chen, T., Wang, F., 2022, Impact assessment of climate change and urbanization on the nonstationarity of extreme precipitation: A case study in an urban agglomeration in the middle reaches of the Yangtze river, *Sustainable Cities and Society*, Volume 85, 2022, 104038, ISSN 2210-6707, https://doi.org/10.1016/j.scs.2022.104038.

Li, W., & Liu, C. H. (2022). On the flow response to an abrupt change in surface roughness. *Flow, Turbulence and Combustion*, 1-23.

Lo, J., Lau, A., Chen, F. and Fung, J. (2007), Urban modification in a mesoscale model and the effects on the local circulation in the Pearl River Delta Region. *J. Appli. Meteorol*. DOI: https://doi.org/10.1175/JAM2477.1

Lemonsu, A., Bastin, S., Masson, V. et al. (2006), Vertical Structure of the Urban Boundary Layer over Marseille Under Sea-Breeze Conditions. *Boundary-Layer Meteorol* 118, 477–501. https://doi.org/10.1007/s10546-005-7772-y

Melecio-Vázquez, D., Ramamurthy, P., Arend, M. et al. (2018), Thermal Structure of a Coastal–Urban Boundary Layer. Boundary-Layer Meteorol 169, 151–161. https://doi.org/10.1007/s10546-018-0361-7

Melas, D., Ziomas, I. C., Zerefos, C. S., (1995) Boundary layer dynamics in an urban coastal environment under sea breeze conditions, *Atmospheric Environment*, 29(24), 3605-3617, https://doi.org/10.1016/1352-2310(95)00140-T.

Meng Q, Liu W, Zhang L, Allam M, Bi Y, Hu X, Gao J, Hu D, Jancsó T. (2022), Relationships between Land Surface Temperatures and Neighboring Environment in Highly Urbanized Areas: Seasonal and Scale Effects Analyses of Beijing, China. *Remote Sensing*.; 14(17):4340. https://doi.org/10.3390/rs14174340

Mestayer, PG, Durand, P, Augustin, P, Bastin, S, Bonnefond, JM, Benech, B, Campistron, B, Coppalle, A, Delbarre, H, Dousset, B, Drobinski, P, Druilhet, A, Frejafon, E, Grimmond, S,

Groleau, D, Irvine, M, Kergomard, C, Kermadi, S, Lagouarde, J-P, Lemonsu, A, Lohou, F, Long, N, Masson, V, Moppert, C, Noilhan, J, Offerle, B, Oke, T, Pigeon, G, Puygrenier, V, Roberts, S, Rosant, JM, Said, F, Salmond, J, Talbaut, M, Voogt, J: (2005), The urban boundary-layer field campaign in Marseille (UBL/CLU-Escompte): set-up and first results. vol. 114, pp. 315-365. Bound-Layer Meteorol. doi: 10.1007/s10546-004-9241-4

Mote, T.L., Lacke, M.C., & Shepherd, J.M. (2007). Radar signatures of the urban effect on precipitation distribution: A case study for Atlanta, Georgia. *Geophysical Research Letters, 34*.

Oke, T. R., Mills, G., Christen, A., & Voogt, J. A. (2017). *Urban Climates* (1st ed.). Cambridge University Press. https://doi.org/10.1017/9781139016476

Pandolfi, M., Martucci, G., Querol, X., Alastuey, A., Wilsenack, F., Frey, S., O'Dowd, C. D., and Dall'Osto, M.: (2013), Continuous atmospheric boundary layer observations in the coastal urban area of Barcelona during SAPUSS, Atmos. Chem. Phys., 13, 4983–4996, https://doi.org/10.5194/acp-13-4983-2013.

Rauber, R. M., & Nesbitt, S. W. (2018). *Radar meteorology: A first course* (First edition). John Wiley & Sons.

Ramamurthy, P., González, J., Ortiz, L., Arend, M., and Moshary, F., 2017, Impact of heatwave on a megacity: an observational analysis of New York City during July 2016, *Environ. Res. Lett.* **12** 054011, https://doi.org/10.1088/1748-9326/aa6e59.

Rosa, M., Haines, K., Cruz, T., Forman, F., (2023), A binational social vulnerability index (BSVI) for the San Diego-Tijuana region: mapping trans-boundary exposure to climate change for just and equitable adaptation planning. *Mitig Adapt Strateg Glob Change* **28**, 12 (2023). https://doi.org/10.1007/s11027-023-10045-w

Rappenglück, B., Perna, R., Zhong, S., and Morris, G. A (2008), An analysis of the vertical structure of the atmosphere and the upper-level meteorology and their impact on surface ozone levels in Houston, Texas, *J. Geophys. Res.-Atmos.*, 113, D17315, https://doi.org/10.1029/2007JD009745.

Shao, W., Kam, J., and Cass, E., (2021). Public Awareness and Perceptions of Drought: A Case Study of Two Cities of Alabama. *Risk, Hazards & Crisis in Public Policy*14, 27–44.https://doi.org/10.1002/rhc3.1224844

Smart, L. S., Vukomanovic, J., Sills, E. O., & Sanchez, G. (2021). Cultural ecosystem services caught in a 'coastal squeeze' between sea level rise and urban expansion. *Global Environmental Change*, *66*, 102209.

Srivastava, M. K., Sarthi, P. P., (2002), Turbulent kinetic energy in the atmospheric surface layer during the summer monsoon Meteorol. Appl. 9, 239–246. DOI:10.1017/S1350482702002098.

Stewart, I. D., & Oke, T. R. (2012). Local climate zones for urban temperature studies. *Bulletin of the American Meteorological Society*, *93*(12), 1879-1900.

Tagtachian, D., & Balk, D. (2023). Uneven vulnerability: Characterizing population composition and change in the low elevation coastal zone in the United States with a climate justice lens, 1990–2020. *Frontiers in Environmental Science,* doi: https://doi.org/10.3389/fenvs.2023.1111856

Wang, J., Feng, J., Yan, Z., Hu, Y., & Jia, G. (2012). Nested high-resolution modeling of the impact of urbanization on regional climate in three vast urban agglomerations in China. *Journal of Geophysical Research: Atmospheres*, *117*(D21).

Yoshikado, H., Kondo, H. Inland penetration of the sea breeze over the suburban area of Tokyo. Boundary-Layer Meteorol 48, 389–407 (1989). https://doi.org/10.1007/BF00123061.